

Distance of PSR B0458+46 indicated by *FAST* HI absorption observations

W. C. Jing,^{1,2} J. L. Han,^{1,2}★ Tao Hong,¹ Chen Wang,^{1,2} X. Y. Gao,^{1,2} L. G. Hou,^{1,2} D. J. Zhou,^{1,2}
J. Xu,¹ Z. L. Yang^{1,2}

¹National Astronomical Observatories, Chinese Academy of Sciences, 20A Datun Road, Chaoyang District, Beijing 100101, China

²School of Astronomy, University of Chinese Academy of Sciences, Beijing 100049, China

Accepted XXX. Received YYY; in original form ZZZ

ABSTRACT

The pulsar B0458+46 was previously believed to have a distance of about 1.3 kpc and to be associated with a nearby supernova remnant, SNR HB9 (G160.9+2.6). We observe the neutral hydrogen (HI) absorption spectrum of PSR B0458+46 by using the *Five-hundred-meter Aperture Spherical radio Telescope* (FAST), and detect two absorption lines at radial velocities of $V_{\text{LSR}} = -7.7 \text{ km s}^{-1}$ and -28.1 km s^{-1} . Based on the Galactic rotation curve with a modification factor correcting for the systematic stream in the Galactic anti-center region, we derive the kinematic distance of the farther absorption cloud, which is found to be located $2.7^{+0.9}_{-0.8}$ kpc away, just beyond the Perseus Arm. We also obtain a direct distance estimation of the farther absorption cloud as being $2.3^{+1.1}_{-0.7}$ kpc, based on a comparison of the velocity with the HI emission in the Perseus and Outer Arms that was well-defined by recently measured parallax tracers. As a result, we conclude that PSR B0458+46 should be located beyond the Perseus Arm, with a lower limit for the distance at 2.7 kpc, and therefore not associated with SNR HB9. The doubled distance indicates a deficiency of thermal electrons in the immediate outer Galaxy, with a much less density than current models predict. Additionally, we detect a new high-velocity HI cloud in the direction of this pulsar.

Key words: pulsars: individual: PSR B0458+46

1 INTRODUCTION

Pulsar distance is a fundamental parameter for several related studies such as population syntheses (e.g. Lorimer et al. 2006) and pulsar luminosity function (e.g. Wu et al. 2020). The distance to a radio pulsar can be inferred from the dispersion measure (DM) by $DM = \int_0^{\text{distance}} n_e ds$ based on a distribution model for electron density n_e , with ds being the unit segment along the line of sight. However, independent measurements of pulsar distances are necessary to construct a reliable model of the Galactic free electron density distribution (e.g. Taylor & Cordes 1993; Cordes & Lazio 2002; Yao et al. 2017). There are three methods for obtaining an independent pulsar distance (Frail & Weisberg 1990; Verbiest et al. 2012): (1) direct parallax measurements of pulsars (e.g. Deller et al. 2019), (2) association with an object of known distance (e.g. Camilo et al. 2002; Lemiére et al. 2009), and (3) kinematic distance of low-latitude pulsars derived from foreground neutral hydrogen (HI) clouds (e.g. Weisberg et al. 1979; van Leeuwen et al. 2015).

Kinematic distance constraints can be obtained from the absorption of pulsar emission by foreground HI clouds (Frail & Weisberg 1990). The distance of an HI cloud located in the Galactic plane can be estimated through a Galactic rotation curve model that converts the measured radial velocity of the cloud into distance (e.g. Blaauw & Schmidt 1965; Fich et al. 1989; Brand & Blitz 1993; Reid et al. 2019). If foreground HI clouds obscure a pulsar, the HI absorption

lines should appear against the emission of that pulsar (e.g. Weisberg et al. 1979, 1980, 2008; Frail & Weisberg 1990), which sets a lower limit on the pulsar distance. Conversely, if a cloud does not produce any absorption, the measurements of the cloud could provide an upper limit for the pulsar distance. The kinematic distance constraints of 62 pulsars have been utilized to model the distribution of free electrons in the Galaxy (e.g. Yao et al. 2017).

To successfully observe and resolve the HI absorption line in pulsar emission, either the pulsar must be strong or the radio telescope must be sensitive enough to achieve a reasonable signal-to-noise (S/N) ratio within an affordable observation time (see, e.g. Frail & Weisberg 1990). The *Five-hundred-meter Aperture Spherical radio Telescope* (FAST, Nan 2006; Nan et al. 2011) is a highly sensitive radio telescope capable of efficiently observing HI absorption spectra better than other telescopes (e.g. Yu et al. 2022).

PSR B0458+46 (J0502+4654) is a pulsar that was first discovered by Damashek et al. (1978) during the early scanning survey of the old 300-feet (91 m) transit radio telescope at Green Bank. It is located in the Galactic disk at the Galactic coordinates of $(l, b) = (160.362^\circ, +3.0766^\circ)$. PSR B0458+46 has a spin period of 0.6386 s and a DM of $41.834 \text{ pc cm}^{-3}$ (see the updated webpage¹ version of Manchester et al. 2005). Its distance is estimated to be about 1.3 kpc according to its DM value using the Galactic electron density model (e.g. Cordes & Lazio 2002; Yao et al. 2017). PSR B0458+46

★ E-mail: hjl@nao.cas.cn (JLH)

¹ <https://www.atnf.csiro.au/people/pulsar/psrcat/>

Table 1. FAST observation parameters for PSR B0458+46.

| | |
|---|---|
| Observational length (s) @ Date | 1260 @ 2022.08.18 1260 @ 2022.08.22 3600 @ 2022.09.17 |
| <i>FAST spectral backend:</i> | |
| Spectral sampling time (s) | 0.1006633 |
| Spectral central frequency (MHz) | 1420 |
| Spectral bandwidth (MHz) | 31.25 |
| Spectral frequency channel number | 65536 |
| Spectral frequency resolution (kHz) | 0.4768 |
| Spectral velocity resolution (km s^{-1}) | 0.1007 |
| Spectral polarization products | XX, YY, X*Y and XY* |
| <i>FAST pulsar backend:</i> | |
| PSR sampling time (μs) | 49.152 |
| PSR frequency range (MHz) | 1000 – 1500 |
| PSR frequency channel number | 2048 |
| PSR polarization products | XX, YY, X*Y and XY* |

is located inside the supernova remnant (SNR) HB9 (G160.9+2.6) in the sky, raising suspicions that the two objects might be physically associated (e.g. [Damashek et al. 1978](#); [Mitra et al. 2003](#); [Leahy & Tian 2007](#)). This SNR is probably very nearby, located within 1 kpc ([Leahy & Tian 2007](#); [Zhao et al. 2020](#)). However, there have been no independent distance measurements for this pulsar.

We use the FAST to observe the HI absorption line of PSR B0458+46. The observations and data processing methods for obtaining the pulsar HI absorption spectrum are described in Section 2. In Section 3, we present the results of our FAST observations. In Section 4, we discuss relevant issues, including the potential association with the SNR HB9 and the electron density distribution in the outer Galactic disk. We summarize our findings in Section 5. As a by-product, we detect a new high-velocity HI cloud in the line of sight of this pulsar, which is presented in the Appendix A.

2 OBSERVATIONS AND DATA REDUCTION

2.1 Observations

We conducted FAST observations of PSR B0458+46 using the central beam of the L-band 19-beam receiver ([Jiang et al. 2020](#)) on August 18 and 22 as the main part of project PT2022_0197, and on September 17 in the context of project ZD2022_2. The observational parameters are summarized in Table 1. Both the spectral backend and pulsar backend were used to simultaneously record data. The receiver covers a frequency range of 1000 – 1500 MHz. At the beginning of every observation session, the calibration signals with an amplitude of $T_{\text{noise}} = 1.1$ K and an on-off period of 2.01326 s are injected to the receiver feed for 2 min, and the data with these calibration signals are recorded for calibrations.

To observe the HI line, we used the N mode of the FAST spectral backend, which splits signals from a bandwidth of 31.25 MHz around 1420 MHz into 65536 frequency channels. This provides a frequency resolution of 0.4768 kHz, corresponding to a velocity resolution of 0.1 km s^{-1} for the HI line. The spectral backend accumulates and saves data every 0.1 s during the observations.

During all observation sessions, we use the FAST pulsar backend to simultaneously record searching-mode data with a time resolution of $49.152 \mu\text{s}$ for 2048 frequency channels that cover the frequency

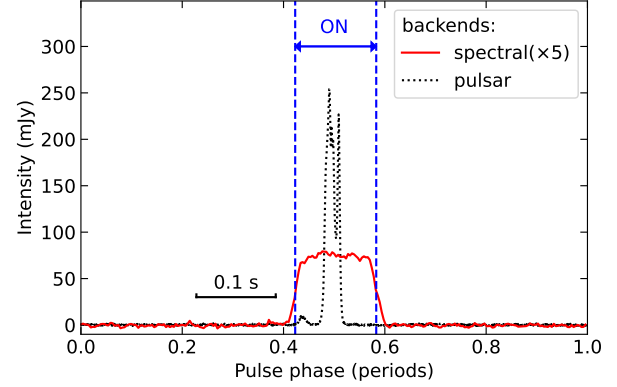


Figure 1. The integrated pulse profiles of PSR B0458+46 obtained from data recorded by the FAST spectral backend (solid line, 256 phase bins per period) and pulsar backend (dot line, 512 phase bins per period). Note that the spectral backend saves data every 0.1 s, equivalently a sample for about 40 phase bins for the solid line. The pulse-on phase range of the folded spectral data is marked by two vertical dashed lines.

range of 1000 – 1500 MHz, each with the 4 polarization products (XX, YY, X*Y and XY*).

2.2 Data Processing

We conducted careful processing of the narrow-band spectral data. First, we manually checked the radio frequency interference (RFI) level for each observation session and found that the data around 1420 MHz were very clean, requiring no RFI mitigation for spectral data. Next, we obtained the intensity calibration factors from the 2-min sub-session with on-off calibration signals. The data were folded with a period of 2.01326 s, and the calibration factors were derived from the machine number differences between the noise-on and noise-off spectra. With such a scale factor, the machine number in real observation data for the total power can be converted to antenna temperature T_A . A pulsar can contribute δT_A to the system temperature. Taking the FAST gain of $G = 16 \text{ K Jy}^{-1}$ (see Table 5 in [Jiang et al. 2020](#)), one can convert the δT_A of pulsar to the mean flux density S_ν with a formula of $S_\nu \times P/W = \delta T_A/G$, where P is the spin period and W is the pulse width.

For velocity calibration, we used the Python package *astropy* ([Astropy Collaboration et al. 2013, 2018](#)) to correct for the Doppler effect induced by the spin and orbit of the Earth, which allowed us to measure radial velocities relative to the barycenter of the solar system. Finally, we modified the barycentric velocity of HI clouds to the velocity V_{LSR} towards the local standard of rest (LSR), by adopting the standard solar motion with 20 km s^{-1} towards RA (1900) of 18^{h} and Dec (1900) $+30^\circ$ (see [Kerr & Lynden-Bell 1986](#)). The values in the Galactic Cartesian frame are $(U_\odot, V_\odot, W_\odot) = (10.0, 15.4, 7.8) \text{ km s}^{-1}$. Here, U_\odot is the velocity towards the Galactic center; V_\odot is parallel with the circular motion of the Galaxy; and W_\odot is towards the northern pole of the Milky Way.

The barycentric period of PSR B0458+46 is calculated from the ephemeris of the pulsar catalog V1.67 ([Manchester et al. 2005](#)), and produces the topocentric period for folding pulses. For each frequency channel, we fold data into 256 phase bins per pulsar period, though one sample of 0.1 s can feed into 40 phase bins. We obtain a waterfall plot in the frequency and pulse phase dimensions. The frequency-integrated pulse profile observed by the spectral backend is shown in Fig. 1, compared with a high time resolution pulse profile

obtained by the pulsar backend folded by DSPSR² (van Straten & Bailes 2011). The broadening of the pulse is caused by the smearing effect of the coarse sampling time of 0.1 s in the FAST spectral backend. According to the integrated profile in Fig. 1, the pulse-on phase is taken as the bins with an intensity greater than the half maximum, and the pulse-off range is taken as the phase range outside 0.4 – 0.6.

In principle, averaging the pulse-on data and pulse-off data from the FAST spectral backend across all spectral channels can produce the pulse-on spectrum and pulse-off spectrum, respectively. However, high resolution spectral measurements can always be affected by standing waves that significantly impact spectral analyses. To obtain the pulsar absorption spectrum, we remove the standing waves naturally by subtracting the averaged pulse-off spectrum from the averaged pulse-on spectrum, which are both affected by the same standing waves. Because the spectral data are well-calibrated, we obtain an absorption spectrum with a satisfactory baseline [see Fig. 2(b) for the sum of three sessions, and Fig. B1 for 3 individual sessions]. Nevertheless, to observe the HI emission line spectrum [see Figure 2(a)], corrections for the standing waves and baseline in the pulse-off spectrum is necessary. We fit the data with a wave model, and obtain good results for each session (see Appendix A for details, demonstrated in Fig. A1), and finally get the HI emission spectrum in Figures 2a.

3 RESULTS AND DISCUSSION

With the measurements for pulse-on and pulse-off temperature and the FAST gain of 16 K Jy^{-1} , we get the flux density of PSR B0458+46 obtained from the well-calibrated different antenna temperatures between pulse-on and pulse-off spectra. PSR B0458+46 was measured by FAST to have mean flux densities of $2.3 \pm 0.3 \text{ mJy}$, $2.4 \pm 0.4 \text{ mJy}$ and $2.5 \pm 0.2 \text{ mJy}$ in three observation sessions. The uncertainty of the flux densities is the root mean square (RMS) of the pulsar spectra around 1420 MHz. The averaged mean flux density at 1.42 GHz measured in the three sessions is $2.4 \pm 0.2 \text{ mJy}$, which agrees with $2.5 \pm 0.1 \text{ mJy}$ at 1.4 GHz given by Lorimer et al. (1995).

The absorption spectrum of PSR B0458+46 is obtained as a weighted-average of the three measurement sessions and is shown in Fig. 2(b). Two absorption lines are detected at radial velocities of $V_{\text{LSR}} = -7.7 \text{ km s}^{-1}$ and -28.1 km s^{-1} . Based on the radial velocity at the absorption center and the modified velocity-distance conversion curve [see Fig. 2(c) and details below], a lower limit for the pulsar distance is estimated to be 2.7 kpc.

In the following, we discuss the results in detail.

3.1 HI emission lines

The HI emission lines in the direction of PSR B0458+46 were previously obtained from available surveys, such as the Effelsberg-Bonn HI survey (i.e., EBHIS, see Winkel et al. 2016). Our new FAST observations have a smaller beam and a better sensitivity, but get similar HI emission lines to the previous data. We normalize the FAST measurements to conform to the precise brightness temperature of T_{B} given by Winkel et al. (2016). The great similarities of the line details are shown in Fig. 2(a) between our new FAST measurement and previous results.

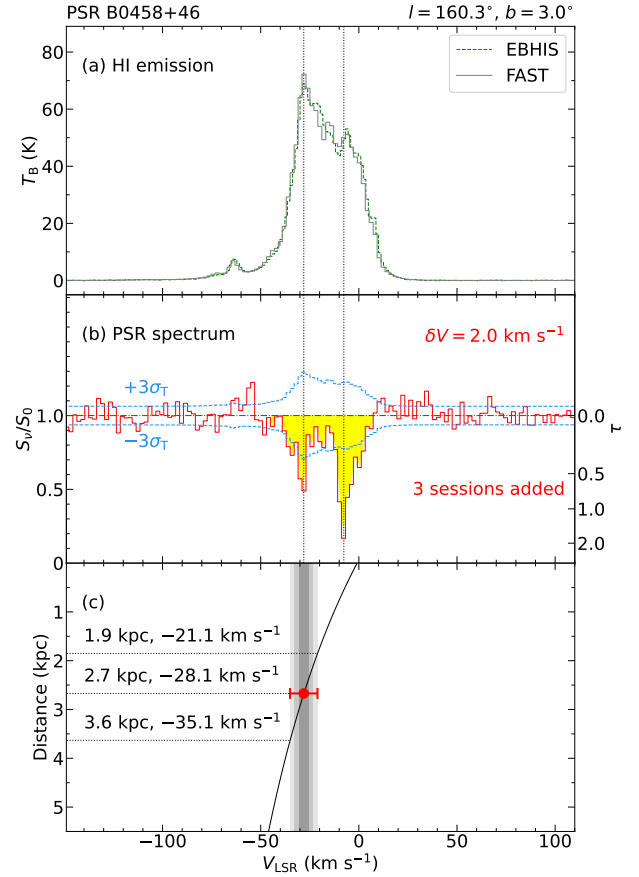


Figure 2. FAST observations of HI lines for determining the lower limit for the distance of PSR B0458+46. (a) *Top subpanel:* The observed HI emission line integrated from all three sessions, compared with the result from the EBHIS (Winkel et al. 2016). (b) *Middle subpanel:* Final HI absorption spectrum of the pulsar, obtained as the weighted sum of three sessions, plotted together with $\pm 3\sigma_{\text{T}}$ lines and the marked absorption line area. The spectrum is scaled by its median unabsorbed value, which is scaled by FAST gain and get $S_0 = 2.4 \text{ mJy}$. The σ_{T} lines are obtained by considering the contributions from HI emission [see equation (B1)]. The opacity τ on the right is derived from $e^{-\tau} = S_v/S_0$. Two vertical dotted lines correspond to the two peaks of absorption lines. (c) *Bottom subpanel:* Velocity-distance conversion for HI clouds on the line of sight of PSR B0458+46, that is derived from the Galactic rotation curve but modified by a factor of 1.6 (see text) caused by the systematic streaming motion in the Galactic anti-center. A gray shadow indicates the velocity probability range caused by the random peculiar motion of HI clouds.

3.2 Pulsar HI absorption spectrum

The pulsar spectrum, showing the HI absorption line of pulsar emission as in Fig. 2(b), is the difference between the spectra gathered in the pulse-on and pulse-off phase ranges. The pulsar spectra obtained during all three observation sessions reveal the presence of two distinct HI absorption lines, as shown in Fig. B1 in Appendix B, probably because the HI clouds in front of the pulsar do not exhibit significant variations (e.g. Stanimirović et al. 2003; Weisberg et al. 2008; Liu et al. 2021) in the time scale of only one month (rather than years). However, the low S/N ratio of each session prevents us from confidently claiming any significant changes in the observed HI absorption lines. To improve the S/N ratio of the HI absorption lines, especially the one with a more negative velocity which comes from distant clouds, we add these results from all three observations

² <http://dspsr.sourceforge.net/>

(Fig. B1) and obtain the finally weighted average for the pulsar HI absorption spectrum as shown in Fig. 2(b). No doubt that two absorption lines are detected at the velocities of $V_{\text{LSR}} = -7.7 \text{ km s}^{-1}$ and -28.1 km s^{-1} , with a S/N ratio of more than $4\sigma_T$ for both. Here σ_T results from the system temperature, plus the extra noise temperature from the strong HI emission in these frequency channels (Weisberg et al. 2008), see Appendix B for details.

Notice that any improper calibration of the pulse-on or pulse-off spectra may leak the strong HI emission line into the final absorption spectrum, which then forms the “ghosts of HI emission” (Weisberg et al. 1980). There is no evidence of this phenomenon in our FAST observation result in Fig. 2(b), probably because (1) the spectral sampling with 0.1 s enables us to resolve the **strongly fluctuating** individual pulses of PSR B0458+46, with 6 samples per period, which enable us to properly separate the phase ranges for pulse-on and pulse-off in every period; (2) both pulse-on and pulse-off spectra are well-scaled; (3) the FAST spectral data have a large dynamic range as they are expressed by 32-bit float; and (4) the baseline and standing waves are the same for both the pulse-on or pulse-off spectra and diminished properly from the spectrum subtraction.

3.3 New distance limit of PSR B0458+46

After the velocities of foreground HI clouds are determined, the kinematic distance of the clouds can be estimated based on the Galactic rotation curve and then the distance of a pulsar can be constrained (e.g. Weisberg et al. 1980; Frail & Weisberg 1990; Weisberg et al. 2008; Verbiest et al. 2012). The conventional rotation curve that constrains pulsar distances is given by Fich et al. (1989) and adopts the International Astronomical Union (IAU) defined parameters of $R_0 = 8.5 \text{ kpc}$ and $\Theta_0 = 220 \text{ km s}^{-1}$, where R_0 is the distance to the Galactic Center and Θ_0 is the rotation speed of the Galaxy at R_0 (Kerr & Lynden-Bell 1986). Note that the peculiar motions of HI clouds in the Perseus Arm and Outer Arm need to be taken into account as they have an additional motion in addition to the circular motion of the rotation curve (see e.g. Reid et al. 2019; Peek et al. 2022), which prevents their distances from being derived directly from the rotation curve. Therefore, it is necessary to modify the velocity-distance conversion in the direction around $l \sim 160^\circ$. We modify the velocity-distance conversion curve by a factor of 1.6 to the observed radial velocities, similarly to what was done for $100^\circ < l < 140^\circ$ (Joncas et al. 1989; Frail & Weisberg 1990). Such a modification can be applied to the longitude-distance curve of each spiral arm from a longitude-velocity curve (e.g. Vallée 2008), so that the newly calculated longitude-velocity curves match the observed spiral arms very well, as shown in in Fig. 3.

Particularly, to estimate the distances of the clouds obscuring PSR B0458+46, this modified velocity-distance conversion is used in Fig. 2(c). An uncertainty caused by possible non-circular and random peculiar motions of clouds with a typical value of 7 km s^{-1} (Dickey & Lockman 1990; Reid et al. 2009; Wienen et al. 2015) is indicated by the shadowed region in Fig. 2(c). The nearby cloud for a peak velocity of $V_{\text{LSR}} = -7.7 \text{ km s}^{-1}$ has a distance of $0.6 \pm 0.6 \text{ kpc}$. The distant cloud with a peak velocity of $V_{\text{LSR}} = -28.1 \text{ km s}^{-1}$ should be at a distance in the range of $[1.9, 3.6] \text{ kpc}$, mostly probably 2.7 kpc. Because the pulsar must be behind the distant cloud, we therefore adopt the lower distance limit of PSR B0458+46 as being $2.7^{+0.9}_{-0.8} \text{ kpc}$. This pulsar is probably located behind the center of the Perseus Arm at 1.9 kpc in this direction (see Fig. 3).

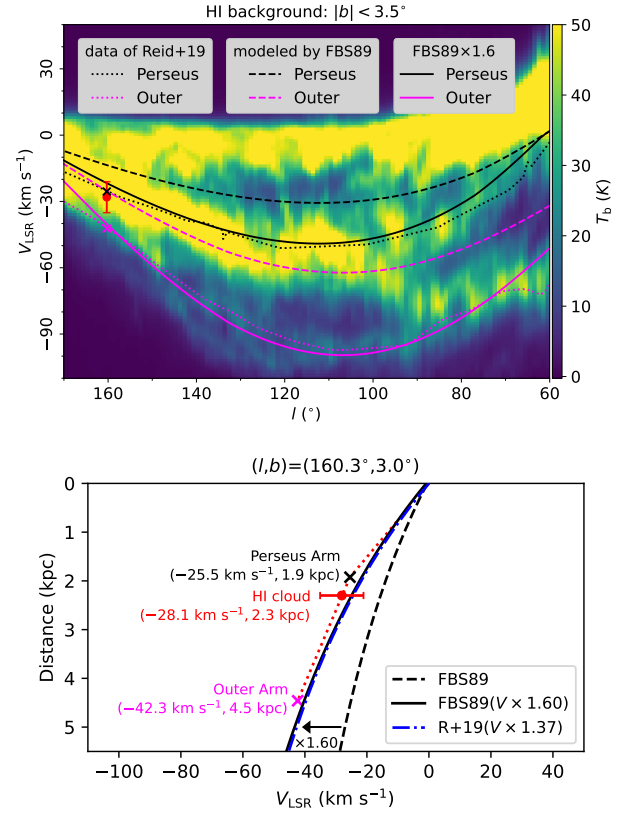


Figure 3. *Top panel:* The background image is the longitude-velocity plot of HI integrated from $|b| < 3.5^\circ$ of EBHIS (Winkel et al. 2016) in the longitude range of $l = 60^\circ$ to 170° . The dotted lines are the Perseus Arm and the Outer Arm outlined according to Reid et al. (2019). The dashed and solid lines represent the velocity-longitude curves calculated from the original and modified velocity-distance conversions, respectively. At the longitude of the pulsar, the red dot denotes the HI absorption of -28.1 km s^{-1} with an error bar of 7 km s^{-1} , while the two crosses indicate the velocities and distances of Perseus and Outer Arms given by Reid et al. (2019). *Bottom panel:* Velocity-distance conversion curves in the direction of the pulsar. The dashed black line represents the original conversion from the conventional rotation curve of Fich et al. (1989), while the solid black line has been modified by a multiplicative factor of 1.60 on the negative velocity (see text). The dash-dotted blue line, which lies virtually atop the solid line, represents the modified conversion from the rotation curve of Reid et al. (2019).

4 DISCUSSIONS

The new distance limit of PSR B0458+46 being $D_{\text{psr}} = 2.7^{+0.9}_{-0.8} \text{ kpc}$ has clear implications on the possible association with SNR HB9 and also the Galactic electron density in the outer Galaxy. Nevertheless, we noticed that Reid et al. (2014, 2019) have measured the parallax-based distances of masers, and developed a new “universal” rotation curve for the Milky Way. We discuss if the use of this revised rotation curve can lead to an alternative distance estimate.

4.1 Alternative distances from an new Galactic rotation curve or simply the HI gas location in arms

The rotation curve of the Milky Way is fundamental for kinematic distance estimation from the observed radial velocities. Recent years new accurate parallax-based measurements of distances of spiral arm tracers have made significant improvements to the Galactic rotation

curve and also R_0 and Θ_0 (Reid et al. 2014, 2019). The adoption of this new rotation curve may lead to more reliable velocity-distance conversions. Among several parameter sets in Reid et al. (2019), the A5 fitting is the best with little-assumed priors, and we adopt a set of self-consistent Galactic parameters from the A5 model for the velocity-distance conversions, in which $\Theta_0 = 236 \pm 7 \text{ km s}^{-1}$ and $R_0 = 8.15 \pm 0.15 \text{ kpc}$ and $(U, V, W) = (10.6 \pm 1.2, 10.7 \pm 6.0, 7.6 \pm 0.7) \text{ km s}^{-1}$.

However, the non-uniform rotation of the Milky Way and the presence of streaming motions have to be cautioned for the velocity-distance conversion. As shown in Fig. 3, the velocity must be multiplied by a factor of 1.37 in the Galactic longitude range of $l = 60^\circ$ to 170° , so that the measured HI gas arms can be consistent with the determined Perseus Arm and outer Arm. We found that with such a factor of 1.37, the velocity-distance conversion is almost the same as that of the conventional rotation curve (Fich et al. 1989) with a factor of 1.60 (see Figure 3). The resulting distance limit by this new conversion is $3.0 \pm 1.0 \text{ kpc}$, which in fact is consistent with the result obtained from the conventional rotation curve (Fich et al. 1989) mainly due to a different factor.

Reid et al. (2016) have demonstrated a technique for calibrating kinematic distance based on the positions of spiral arms, although it differs slightly from the method presented here. The association between velocities of known sources and the HI absorption lines presents an invaluable tool for distance determination, complementing with parallax-based measurements of spiral arm and the gas kinematic distances derived from Galactic rotation curves. As shown in Fig. 3, the absorption line observed at a velocity of -28.1 km s^{-1} matches the velocity for the outer side of the Perseus Arm, which directly suggests that the HI cloud obscuring PSR B0458+46 is likely associated with the Perseus Arm centered at approximately $1.9 \pm 0.2 \text{ kpc}$ away along the line of sight (Xu et al. 2006; Reid et al. 2019). In fact, a cloud at a distance of $2.3^{+1.1}_{-0.7} \text{ kpc}$ can be directly derived for the velocity of -28.1 km s^{-1} from the interpolation of the locations for the Perseus and Outer Arms in this direction as shown Fig. 3, without involving any rotation curve model, since there are the excellent measurements of the location of two spiral arms (Xu et al. 2006; Reid et al. 2019).

4.2 The association between PSR B0458+46 and SNR HB9

PSR B0458+46 is located within the sky area of SNR HB9, leading to a possibility of physical association between the two objects. However, the physical association cannot be determined without verifying the distances of the two objects.

Various methods have been employed to estimate the distance of SNR HB9. In the early days, Caswell & Lerche (1979) derived the relation between the SNR surface brightness Σ and the diameter D for a number of SNRs, and got a distance of 1.8 kpc for SNR HB9. Milne (1979) also found a $\Sigma - D$ relation and suggested the distance of 1.3 kpc for the SNR. Analyzing the H α lines surrounding the SNR, Lozinskaya (1981) got an estimated value of $2 \pm 0.8 \text{ kpc}$ derived from the velocity V_{LSR} of $-18 \pm 10 \text{ km s}^{-1}$ of H α filaments. Investigating the early X-ray observation of that SNR, Leahy & Aschenbach (1995) estimated the distance as 1.5 kpc using the evaporative cloud model. Based on the morphological relevance of the radio image of the SNR and the frequency channel maps in the velocity range of $-3 < V_{\text{LSR}} < -9 \text{ km s}^{-1}$ of HI emission in the new HI surveys, Leahy & Tian (2007) concluded the distance of SNR HB9 is $0.8 \pm 0.4 \text{ kpc}$. Sezer et al. (2019) analyzed the X-ray, gamma-ray and radio images of the SNR, and also verified the HI morphology of different velocities

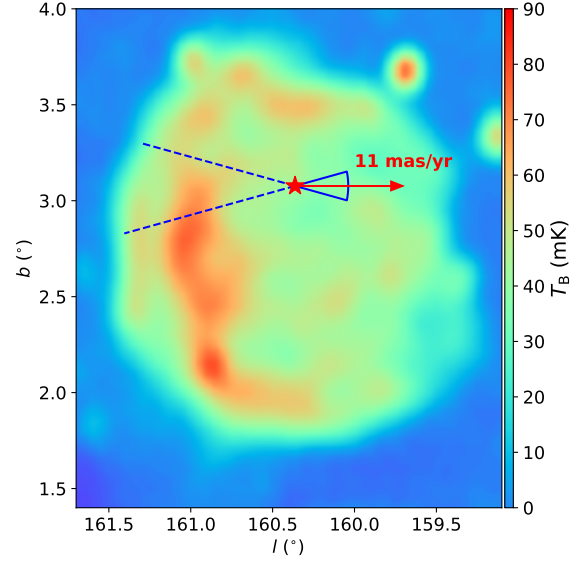


Figure 4. PSR B0458+46 (the star) on the radio emission map of the SNR HB9 produced by the 6-cm survey data of Gao et al. (2010). The proper motion of PSR B0458+46 (Harrison et al. 1993) is indicated by a solid arrow, with its uncertainty indicated by a blue fan-shaped region and a suggested previous location between dashed lines.

from the new HI surveys, and concluded that the distance to the SNR HB9 is $0.6 \pm 0.3 \text{ kpc}$. Ranasinghe & Leahy (2022) recently revised it to $0.7 \pm 0.4 \text{ kpc}$. By observing the extinction of stars, Zhao et al. (2020) suggested a distance of $0.54 \pm 0.10 \text{ kpc}$.

Considering the more recent and improved data, it is evident that the distance to SNR HB9 should be less than 1.0 kpc . Thus, the much closer distance of SNR HB9 compared to the larger distance of PSR B0458+46 indicates that they are not physically associated.

Furthermore, the observed proper motion of PSR B0458+46 also does not support the physical association. Its proper motion has been measured by the very long baseline interferometry (VLBI, Harrison et al. 1993): $\mu_\alpha = -8 \pm 3 \text{ mas yr}^{-1}$, $\mu_\delta = 8 \pm 5 \text{ mas yr}^{-1}$, and timing (Hobbs et al. 2004): $\mu_\alpha \cos(\delta) = 1 \pm 8 \text{ mas yr}^{-1}$, $\mu_\delta = 42 \pm 19 \text{ mas yr}^{-1}$. Because the error bars of the VLBI measurement are much smaller than those of timing, a moving direction and the uncertainty from the VLBI are adopted. The possible region for the birthplace of PSR B0458+46 can be traced back as shown in Fig. 4, apparently too far away from the geometric center of the SNR.

4.3 Electron density in the Outer Disk

Using a lower distance limit of $D_L = 2.7 \text{ kpc}$ and a DM of $41.834 \text{ pc cm}^{-3}$, the mean electron density between PSR B0458+46 and Earth (n_e) is determined to be less than $\text{DM}/D_L = 41.834/2700 = 0.0155 \text{ cm}^{-3}$ as depicted in Fig. 5. This result is significantly lower than the values previously predicted by models of the Galactic electron density distribution (Cordes & Lazio 2002; Yao et al. 2017), indicating the deficiency of electrons in the immediate outer Galaxy in the anti-center region.

To verify the electron density distribution in different parts of our Galaxy, e.g. in the spiral arms and inter-arm regions, in the central bulge and anti-center region, we need to measure the dispersion of pulsed signals and the distance of many pulsars. The latter is challenging to achieve, as demonstrated by this work.

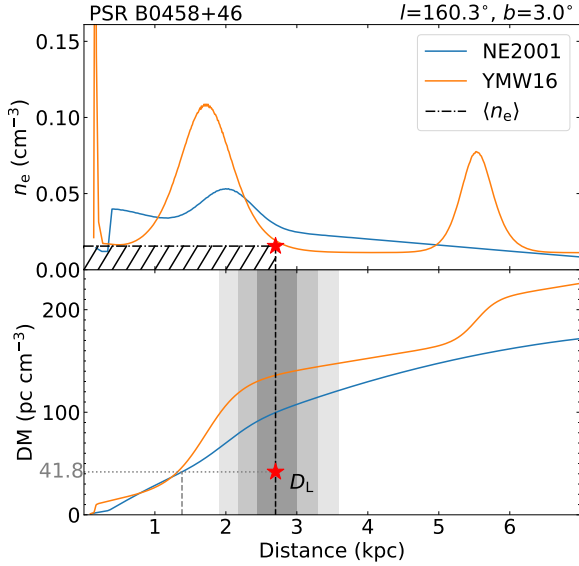


Figure 5. *Top panel:* Electron density along the line of sight to PSR B0458+46 in the Galactic electron density models, NE2001 (Cordes & Lazio 2002) and YMW16 (Yao et al. 2017). The area of the hatched rectangle bounded by the lower distance limit and the associated mean electron density must be equal (by definition) to the dispersion measure. The corresponding areas under the two modeled electron density curves are much higher. *Bottom panel:* Comparison of the DM of PSR B0458+46 with model predictions. The shadowed area stands for possible range of pulsar distance, caused by the random cloud motion of 7 km s^{-1} .

5 SUMMARY

By using the FAST, we observe the HI absorption lines from the foreground clouds in front of PSR B0458+46. The two absorption lines were detected at velocities of -7.7 and -28.1 km s^{-1} , respectively. Using the conventional Galactic rotation curve (Fich et al. 1989) and accounting for the modification on its velocity-distance conversion near the Galactic anti-center (Frail & Weisberg 1990), the most probable distance of the farthest foreground HI cloud in front of this pulsar is around 2.7 kpc . We try to use the new derived rotation curve of Reid et al. (2019) but with a different modification factor to account the streaming motions in the Galactic anti-center, and get a similar distance. In fact, the direct interpolation of the HI gas velocities in the parallax-based spiral arms for the absorption clouds with a velocity of -28.1 km s^{-1} gives a distance of 2.3 kpc . we take 2.7 kpc as the lower distance limit of PSR B0458+46 with three reasons: 1) it is consistent with previous standard procedures; 2) it is between the $3.0 \pm 1.0 \text{ kpc}$ and $2.3^{+1.1}_{-0.7} \text{ kpc}$ in Section 4.1; 3) all of them are consistent in the uncertainty. We therefore conclude that PSR B0458+46 must be located behind the Perseus arm and not physically associated with SNR HB9. The larger distance of PSR B0458+46 implies a much lower electron density in the anti-center region, indicating the deficiency of electrons in the immediate outer Galaxy.

Such a new measurement of HI absorption lines of pulsars by the sensitive FAST observations demonstrates the FAST capability of constraining new kinematic distances of pulsars and contributing to improve the Galactic electron density distribution model in the near future.

ACKNOWLEDGEMENTS

Sincere thanks to the expert referee, Prof. Joel M. Weisberg for the generous, inspiring and kind suggestions and comments. FAST is a Chinese national mega-science facility built and operated by the National Astronomical Observatories, Chinese Academy of Sciences. This work is supported by the National Natural Science Foundation of China (NSFC, Nos. 11988101 and 11833009) and the Key Research Program of the Chinese Academy of Sciences (Grant No. QYZDJ-SSW-SLH021). In addition, TH is supported by the NSFC No. 12003044; CW is partially supported by NSFC No. U1731120; XYG acknowledges the financial support from the CAS-NWO co-operation programme (Grant No. GJHZ1865) and the NSFC No. U1831103; LGH thanks the support from the Youth Innovation Promotion Association CAS; DJZ is supported by the Cultivation Project for the FAST scientific Payoff and Research Achievement of CAMS-CAS; JX is partially supported by NSFC No. U2031115 and the National SKA program of China (Grant No. 2022SKA0120103).

In the data processing, the python packages scipy (Virtanen et al. 2020) and numpy (Harris et al. 2020) are employed.

DATA AVAILABILITY

Original FAST observation data can be accessible in the FAST Data Center one year after observations. All processed data as plotted in this paper, including these in appendix, can be obtained from the authors with a kind request. The pulsar profile data are available for <http://zmtt.bao.ac.cn/psr-fast/>.

REFERENCES

- Astropy Collaboration et al., 2013, *A&A*, **558**, A33
- Astropy Collaboration et al., 2018, *AJ*, **156**, 123
- Blaauw A., Schmidt M., 1965, Galactic structure. University of Chicago Press
- Brand J., Blitz L., 1993, *A&A*, **275**, 67
- Camilo F., et al., 2002, *ApJ*, **571**, L41
- Caswell J. L., Lerche I., 1979, *MNRAS*, **187**, 201
- Cordes J. M., Lazio T. J. W., 2002, arXiv e-prints, [pp astro-ph/0207156](https://arxiv.org/abs/ppastro-ph/0207156)
- Damashek M., Taylor J. H., Hulse R. A., 1978, *ApJ*, **225**, L31
- Deller A. T., et al., 2019, *ApJ*, **875**, 100
- Dickey J. M., Lockman F. J., 1990, *ARA&A*, **28**, 215
- Fich M., Blitz L., Stark A. A., 1989, *ApJ*, **342**, 272
- Frail D. A., Weisberg J. M., 1990, *AJ*, **100**, 743
- Gao X. Y., et al., 2010, *A&A*, **515**, A64
- Han J. L., et al., 2021, *Research in Astronomy and Astrophysics*, **21**, 107
- Harris C. R., et al., 2020, *Nature*, **585**, 357
- Harrison P. A., Lyne A. G., Anderson B., 1993, *MNRAS*, **261**, 113
- Hobbs G., Lyne A. G., Kramer M., Martin C. E., Jordan C., 2004, *MNRAS*, **353**, 1311
- Hong T., Han J., Hou L., Gao X., Wang C., Wang T., 2022, *Science China Physics, Mechanics, and Astronomy*, **65**, 129702
- Jiang P., et al., 2020, *Research in Astronomy and Astrophysics*, **20**, 064
- Joncas G., Roger R. S., Dewdney P. E., 1989, *A&A*, **219**, 303
- Kerr F. J., Lynden-Bell D., 1986, *MNRAS*, **221**, 1023
- Leahy D. A., Aschenbach B., 1995, *A&A*, **293**, 853
- Leahy D. A., Tian W. W., 2007, *A&A*, **461**, 1013
- Lemiere A., Slane P., Gaensler B. M., Murray S., 2009, *ApJ*, **706**, 1269
- Liu M., et al., 2021, *ApJ*, **911**, L13
- Lorimer D. R., Yates J. A., Lyne A. G., Gould D. M., 1995, *MNRAS*, **273**, 411
- Lorimer D. R., et al., 2006, *MNRAS*, **372**, 777
- Lozinskaya T. A., 1981, *Soviet Astronomy Letters*, **7**, 17
- Manchester R. N., Hobbs G. B., Teoh A., Hobbs M., 2005, *AJ*, **129**, 1993
- Milne D. K., 1979, *Australian Journal of Physics*, **32**, 83

Mitra D., Wielebinski R., Kramer M., Jessner A., 2003, *A&A*, **398**, 993
 Nan R., 2006, *Science in China: Physics, Mechanics and Astronomy*, **49**, 129
 Nan R., et al., 2011, *International Journal of Modern Physics D*, **20**, 989
 Peek J. E. G., Tchernyshyov K., Miville-Deschenes M.-A., 2022, *ApJ*, **925**, 201
 Ranasinghe S., Leahy D., 2022, *ApJ*, **940**, 63
 Reid M. J., et al., 2009, *ApJ*, **700**, 137
 Reid M. J., et al., 2014, *ApJ*, **783**, 130
 Reid M. J., Dame T. M., Menten K. M., Brunthaler A., 2016, *ApJ*, **823**, 77
 Reid M. J., et al., 2019, *ApJ*, **885**, 131
 Sezer A., Ergin T., Yamazaki R., Sano H., Fukui Y., 2019, *MNRAS*, **489**, 4300
 Soler J. D., et al., 2022, *A&A*, **662**, A96
 Stanimirović S., Weisberg J. M., Hedden A., Devine K. E., Green J. T., 2003, *ApJ*, **598**, L23
 Taylor J. H., Cordes J. M., 1993, *ApJ*, **411**, 674
 Vallée J. P., 2008, *AJ*, **135**, 1301
 Verbiest J. P. W., Weisberg J. M., Chael A. A., Lee K. J., Lorimer D. R., 2012, *ApJ*, **755**, 39
 Virtanen P., et al., 2020, *Nature Methods*, **17**, 261
 Wakker B. P., van Woerden H., 1997, *ARA&A*, **35**, 217
 Weisberg J. M., Boriakoff V., Rankin J., 1979, *A&A*, **77**, 204
 Weisberg J. M., Rankin J., Boriakoff V., 1980, *A&A*, **88**, 84
 Weisberg J. M., Stanimirović S., Xilouris K., Hedden A., de la Fuente A., Anderson S. B., Jenet F. A., 2008, *ApJ*, **674**, 286
 Wienen M., et al., 2015, *A&A*, **579**, A91
 Winkel B., Kerp J., Flöer L., Kalberla P. M. W., Ben Bekhti N., Keller R., Lenz D., 2016, *A&A*, **585**, A41
 Wu Q.-D., Zhi Q.-J., Zhang C.-M., Wang D.-H., Ye C.-Q., 2020, *Research in Astronomy and Astrophysics*, **20**, 188
 Xu Y., Reid M. J., Zheng X. W., Menten K. M., 2006, *Science*, **311**, 54
 Yao J. M., Manchester R. N., Wang N., 2017, *ApJ*, **835**, 29
 Yu Q., Fang T., Feng S., Zhang B., Xu C. K., Wang Y., Hao L., 2022, *ApJ*, **934**, 114
 Zhao H., Jiang B., Li J., Chen B., Yu B., Wang Y., 2020, *ApJ*, **891**, 137
 van Leeuwen J., et al., 2015, *ApJ*, **798**, 118
 van Straten W., Bailes M., 2011, *Publ. Astron. Soc. Australia*, **28**, 1

APPENDIX A: THE BASELINE AND STANDING-WAVE FITTING AND A HIGH-VELOCITY HI CLOUD

There is a new HI emission line at the velocity of -190 km s^{-1} clearly detected by FAST observations, as shown in the bottom panel of Fig. A1. Data from the EBHIS are shown together for comparison.

To verify the detection, we present and check the raw spectra from XX and YY polarization products of all three observation sessions in the top of Fig. A1. Though the standing waves and baselines are different for each session, the HI line for this high-velocity HI cloud presents in all spectra. Therefore, the cloud revealed by this weak high-velocity line is a true detection.

In general, the standing waves and baseline can be removed by a model-fitting to the line-off region of the pulse-off spectrum with:

$$T_A(V_{\text{LSR}}) = T_{\text{SW}} \sin(\omega_0 V_{\text{LSR}} + \omega_1 V_{\text{LSR}}^2 + \phi) + k \cdot V_{\text{LSR}} + T_0, \quad (\text{A1})$$

here the parameters k and T_0 are set for the linear term, and T_{SW} , ω_0 , ω_1 and ϕ are set for the waves along V_{LSR} .

This newly detected emission line should come from a distant or high-velocity HI cloud (as reviewed by Wakker & van Woerden 1997), similar with the clouds pointed out in the Appendix D of Soler et al. (2022). Such a cloud can be investigated by the piggy-back recorded spectral data during the FAST GPPS survey (Han et al. 2021), as done by Hong et al. (2022).

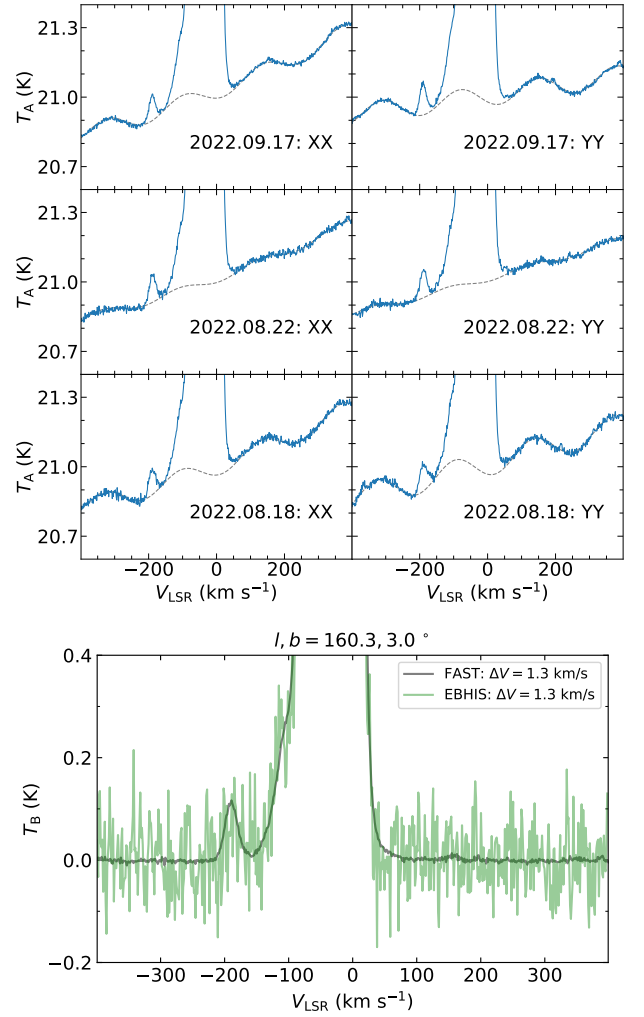


Figure A1. FAST detected HI emission lines in the resolution of 1.3 km s^{-1} with and without subtraction of the standing waves and baselines, zoomed to show the details. In the top panels, the sinusoidal-like baselines on the HI spectra are shown for XX and YY polarization in three observation sessions, respectively. The baseline-removed and summed result is shown in the bottom panel and compared with that from the EBHIS (Winkel et al. 2016). A high-velocity HI cloud is detected at the velocity of around -190 km s^{-1} by the FAST observation.

APPENDIX B: DETECTION OF PULSAR HI ABSORPTION IN THREE SESSIONS

We present the detected absorption in three observation sessions in Fig. B1. All three pulsar spectra show the two absorption lines clearly. Due to the strength of the HI line, the radiometer noise in the on-HI-line portion of a spectrum is enhanced with respect to the noise in the off-line portion of the same spectrum (Weisberg et al. 2008). The noise, in the temperature units, at any frequency f , is given by

$$\sigma_T(f) = \frac{T_{\text{sys}} + T_{\text{HI}}(f)}{\sqrt{n_p t_{\text{int}} \Delta f}}, \quad (\text{B1})$$

where T_{sys} is measured system temperature, T_{HI} is HI temperature, $n_p = 2$ is the number of the polarization probes, t_{int} is the observational time of the pulse-on spectra, and Δf is the frequency resolution of the pulsar spectra. The system temperature is $T_{\text{sys}} \approx 20 \text{ K}$ (Jiang et al. 2020), and the temperature of HI lines $T_{\text{HI}}(f)$ shown in Fig. 2(a)

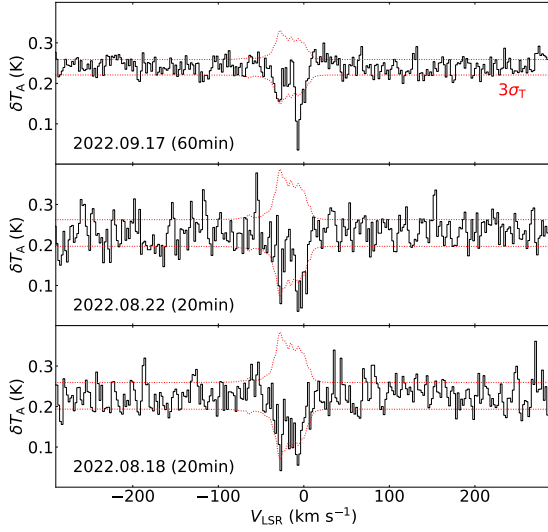


Figure B1. Pulsar spectra obtained in three observational sessions, showing the absorption lines. The thin dot line represents the fluctuations caused by the system temperature and extra temperature from HI emission lines.

is about 40 – 70 K, and then fluctuations due to “system” temperature are therefore enlarged as shown in Fig. B1 and also Fig. 2(b).

This paper has been typeset from a \LaTeX file prepared by the author.